CHEMISTRY OF MATERIALS

Article

pubs.acs.org/cm

Modeling Off-Stoichiometry Materials with a High-Throughput Ab-Initio Approach

Kesong Yang,[†] Corey Oses,[‡] and Stefano Curtarolo*[,‡,§]

[†]Department of NanoEngineering, University of California San Diego, La Jolla, California 92093-0448, United States

[‡]Center for Materials Genomics and [§]Materials Science, Electrical Engineering, Physics and Chemistry, Duke University, Durham, North Carolina 27708, United States

Supporting Information

ABSTRACT: Predicting material properties of off-stoichiometry systems remains a long-standing and formidable challenge in rational materials design. A proper analysis of such systems by means of a supercell approach requires the exhaustive consideration of all possible superstructures, which can be a time-consuming process. On the contrary, the use of quasirandom approximants, although very computationally effective, implicitly bias the analysis toward disordered states with the lowest site correlations. Here, we propose a novel framework designed specifically to investigate stoichiometrically driven trends of disordered systems (i.e., having partial occupation and/or disorder in the atomic sites). At the heart of the approach is the identification and analysis of unique supercells of a virtually equivalent stoichiometry to the disordered material. We employ Boltzmann statistics to resolve system-wide properties at a high-throughput (HT) level. To maximize efficiency and accessibility, we integrated the method within the automatic HT computational framework AFLOW. As proof of concept, we apply our approach to three systems of interest, a zinc chalcogenide ($ZnS_{1-x}Se_x$), a wide-gap oxide semiconductor ($Mg_xZn_{1-x}O$), and an iron alloy ($Fe_{1-x}Cu_x$), at various stoichiometries. These systems exhibit properties that are highly tunable as a function of composition, characterized by optical bowing and linear ferromagnetic behavior. Not only are these qualities successfully predicted, but additional insight into underlying physical mechanisms is revealed.

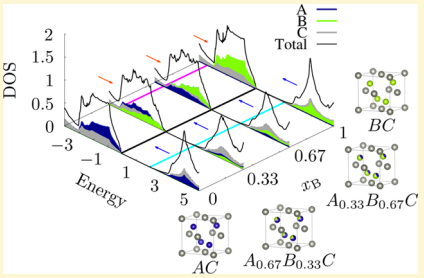

1. INTRODUCTION

Crystals are characterized by their regular, repeating structures. Such a description allows us to reduce our focus from the macroscopic material to a microscopic subset of unique atoms and positions. A full depiction of material properties, including mechanical, electronic, and magnetic features, follows from an analysis of this primitive lattice. First-principles quantum mechanical calculations have been largely successful in reproducing ground state properties of perfectly ordered crystals.[1−3] However, such perfection does not exist in nature. Instead, crystals display a degree of randomness, or disorder, in their lattices. There are several types of disorder, including topological, spin, substitutional, and vibrational.[4] This work focuses on substitutional disorder in which crystallographically equivalent sites of a crystal are not uniquely or fully occupied. Rather, each site is characterized by a statistical, or partial, occupation. Such disorder is intrinsic in many technologically significant systems, including those used in fuel cells,[5] solar cells,[6] high-temperature superconductors,[7,8] low thermal conductivity thermoelectrics,[9] imaging and communications devices,[10] as well as promising rare-earth free materials for use in sensors, actuators, energy harvesters, and spintronic devices.[11] Hence, a comprehensive computational study of substitutionally disordered materials at the atomic scale is of paramount importance for optimizing key physical properties of materials in technological applications.

Unfortunately, structural parameters with partial occupancy cannot be used directly in first-principles calculations—a significant hindrance for computational studies of disordered systems. Therefore, additional efforts must be made to model disorder or aperiodicity.[12−14] Some of the more traditional methods include the virtual crystal approximation,[15−17] coherent potential approximation[18] (and variants that work within the Korringa−Kohn−Rostoker formalism[19−22] and consider nonlocal effects[23]), and special quasirandom structures.[24,25] A rigorous statistical treatment of substitutional disorder at the atomic scale requires utility of large-ordered supercells containing a composition consistent with the compound's stoichiometry.[26−33] However, the computational cost of such large supercell calculations has traditionally inhibited their use. Fortunately, the emergence of high-throughput (HT) computational techniques[3] coupled with the exponential growth of computational power is now allowing the study of disordered systems from first principles.[34]

Herein, we present an approach to perform such a treatment working within the HT computational framework AFLOW.[35,36] We highlight three novel and attractive features central to this method: complete implementation into an automatic high-

Received: April 13, 2016
Revised: July 31, 2016
Published: August 22, 2016

DOI: 10.1021/acs.chemmater.6b01449
Chem. Mater. 2016, 28, 6484−6492

Table 1. Evolution of the Algorithm Used to Optimize the Partial Occupancy Values and Superlattice Size for the Disordered System $Ag_{8.733}Cd_{3.8}Zr_{3.267}$[a]

	occup. one (Ag)		occup. two (Zr)		occup. three (Cd)			
n'	f_1	e_1	f_2	e_2	f_3	e_3	e_{max}	n
1	1/1	0.2670	0/1	0.2670	1/1	0.2000	0.2670	1
2	1/2	0.2330	1/2	0.2330	2/2	0.2000	0.2330	2
3	2/3	0.0663	1/3	0.0663	2/3	0.1333	0.1333	3
4	3/4	0.0170	1/4	0.0170	3/4	0.0500	0.0500	4
5	4/5	0.0670	1/5	0.0670	4/5	0.0000	0.0670	5
6	4/6	0.0663	2/6	0.0663	5/6	0.0333	0.0663	6
7	5/7	0.0187	2/7	0.0187	6/7	0.0571	0.0571	7
8	6/8	0.0170	2/8	0.0170	6/8	0.0500	0.0500	4
9	7/9	0.0448	2/9	0.0448	7/9	0.0222	0.0448	9
10	7/10	0.0330	3/10	0.0330	8/10	0.0000	0.0330	10
11	8/11	0.0057	3/11	0.0057	9/11	0.0182	0.0182	11
12	9/12	0.0170	3/12	0.0170	10/12	0.0333	0.0333	12
13	10/13	0.0362	3/13	0.0362	10/13	0.0308	0.0362	13
14	10/14	0.0187	4/14	0.0187	11/14	0.0143	0.0187	14
15	11/15	0.0003	4/15	0.0003	12/15	0.0000	0.0003	15

[a] f_i indicates the iteration's choice fraction for each partially occupied site (i = 1, 2, 3, ...); e_i indicates the error between the iteration's choice fraction and the actual partial occupancy value. e_{max} is the maximum error of the system.

throughput framework (optimizing speed without mitigating accuracy), utility of a novel occupancy optimization algorithm, and use of the Universal Force Field method[37] to reduce the number of DFT calculations needed per system.

To illustrate the effectiveness of the approach, we apply it to three disordered systems, a zinc chalcogenide ($ZnS_{1-x}Se_x$), a wide-gap oxide semiconductor ($Mg_xZn_{1-x}O$), and an iron alloy ($Fe_{1-x}Cu_x$), and successfully reproduce experimental results while predicting new phenomena:

- We resolve $ZnS_{1-x}Se_x$ to show a small yet smooth optical bowing over the complete compositional space. Additionally, we can conclude that this system is of the amalgamation type and not of the persistence type by observing the stoichiometrically evolving ensemble average DOS.
- We find $Mg_xZn_{1-x}O$ to exhibit an abrupt transition in optical bowing consistent with a phase transition over its compositional range.
- We predict the ferromagnetic behavior of $Fe_{1-x}Cu_x$ to be smoothly stifled as more copper is introduced into the structure, even through a phase transition.
- We justify the thermodynamic properties for the three aforementioned disordered systems through an analysis of the mixing energies of the enumerated structures.

Through our approach, these features are not only recovered, but additional insight into the underlying physical mechanisms is also retrievable.

2. METHODOLOGY

This section details the technicalities of representing a partially occupied disordered system as a series of unique supercells. Here is an outline of the approach:

(1) For a given disordered material, optimize its partial occupancy values and determine the size of its derivative superlattices (section 2.1).

(2) (a) Use superlattice size n to generate a set of unique derivative superlattices and corresponding sets of unique supercells with the required stoichiometry and (b) import these nonequivalent supercells into the automatic computational framework AFLOW for HT first-principles electronic structure calculations (section 2.2).

(3) Obtain and use the relative formation enthalpy $\Delta H_{F,i}$ to calculate the equilibrium probability of each supercell P_i as a function of temperature T according to the Boltzmann distribution (section 2.3).

(4) Determine the disordered system's material properties through ensemble averages of the properties calculated for each supercell. Specifically, we will calculate the system's density of states (DOS), band gap energy E_{gap}, and magnetic moment M (section 2.4).

In the following sections, we will refer to a model disordered system, $Ag_{8.733}Cd_{3.8}Zr_{3.267}$, to illustrate the technical procedures mentioned above. This disordered system has two partially occupied sites: one shared between silver and zirconium and another shared between cadmium and a vacancy. Working within the AFLOW framework,[38] we have designed a simple structure file for partially occupied systems. Adapted from VASP's POSCAR,[39,40] `PARTCAR` contains within it a description of lattice parameters and a list of site coordinates and occupants along with a concentration tolerance (explained in the next section) and (partial) occupancy values for each site. For more details about this structure or its `PARTCAR`, please see the Supporting Information.

2.1. Determine Superlattice Size. To fully account for the partial occupancy of the disordered system, we should generate a set of superlattices of a size corresponding to the lowest common denominator of the fractional partial occupancy values. With partial occupancy values of 0.733 (733/1000) and 0.267 (267/1000) in disordered system $Ag_{8.733}Cd_{3.8}Zr_{3.267}$, we would need to construct superlattices of size 1000. Not only would we be working with correspondingly large supercells (16,000 atoms per supercell in our example), but the number of unique supercells in the set would be substantial. This would extend well beyond the capabilities of first-principles calculations and thus is not practical. It is therefore necessary to optimize the partial occupancy values to produce an appropriate superlattice size.

We demonstrate the utility of an efficient algorithm to calculate the optimized partial occupancy values and corresponding superlattice size with our example disordered system $Ag_{8.733}Cd_{3.8}Zr_{3.267}$ in Table 1. For convenience, we refer to the algorithm's iteration step as n', the superlattice index, and n as the superlattice size. Quite simply, the algorithm iterates, increasing the superlattice index from 1 to n' until the optimized partial occupancy values reach the required accuracy. At each iteration, we generate a fraction for each partially occupied site, all of which have the common denominator n'. The numerator is determined to be the integer that reduces the overall fraction's error relative to the actual site's fractional partial occupancy value. The superlattice size corresponds to the lowest common denominator of the irreducible fractions (e.g., see iteration step 8). The maximum

DOI: 10.1021/acs.chemmater.6b01449
Chem. Mater. 2016, 28, 6484−6492

error among all of the sites is chosen to be the accuracy metric for the system.

For disordered system $Ag_{8.733}Cd_{3.8}Zr_{3.267}$, given a tolerance of 0.01, the calculated superlattice size is 15 (240 atoms per supercell). By choosing a superlattice with a nearly equivalent stoichiometry as the disordered system, we have reduced our supercell size by over a factor of 60 and entered the realm of feasibility with this calculation.

Quite expectedly, we see that the errors in partial occupancy values calculated for silver and zirconium are the same, as they share the same site. The same holds true for cadmium and its vacant counterpart (not shown). Therefore, the algorithm only needs to determine one choice fraction per site instead of per occupant (as shown). Such an approach reduces computational costs by guaranteeing that only the smallest supercells (both in number and size) with the lowest tolerable error in composition are funneled into our HT first-principles calculation framework.

It is worth mentioning that it may be advantageous to explore superlattices that are larger than necessary, as small supercells may exhibit a high degree of translational symmetry despite having the exact composition. For this reason, the superlattice size is a tunable parameter in the PARTCAR. We highlight the gains from such an approach in section 3.3 with the magnetic moment M. Additionally, we explore the variation of the band gap energy E_{gap} as a function of the superlattice size n in the Supporting Information.

2.2. Unique Supercells Generation. With the optimal superlattice size n, the unique derivative superlattices of the disordered system can be generated using Hermite Normal Form (HNF) matrices.[41] Each HNF matrix generates a superlattice of a size corresponding to its determinant n. There exists many HNF matrices with the same determinant, each creating a variant superlattice. For each unique superlattice, we generate a complete set of possible supercells with the required stoichiometry by exploring all possible occupations of partially occupied sites. However, not all of these combinations are unique, nominally warranting an involved structure comparison analysis that becomes extremely time-consuming for large supercells.[41] Instead, we identify duplicates by estimating the total energy of each supercell in an HT manner based on the Universal Force Field (UFF) method.[37] This classical molecular mechanics force field approximates the energy of a structure by considering its composition, connectivity, and geometry, for which parameters have been tabulated. Specifically, its implementation within AFLOW considers the bond stretch interaction (harmonic oscillator) as well as nonbonded interactions (van der Waals forces). Only supercells with the same total energy are structurally compared and potentially treated as duplicate structures to be discarded if necessary. The count of duplicate structures determines the degeneracy of the structure. Although the UFF method yields a satisfactory sampling of structures for the examples explored in this work (section 3), this component of the framework can be adapted as faster, more efficient enumeration methods are developed.[42−46]

Only nonequivalent supercells are imported into the automatic computational framework AFLOW for HT quantum mechanics. The calculation procedures, including accuracy thresholds, calculation pathways, and mesh dimensions, are in general compliance with the AFLOW Standard.[35] For supercells, the number of k-points per reciprocal atom N_{KPPRA} is set to 1000 and 3000 for the relaxing and static stages of the calculation, respectively.

2.3. Supercell Equilibrium Probability Calculation. The unique supercells representing a partially occupied disordered material are labeled as S_1, S_2, S_3, ..., S_n. Their formation enthalpies (per atom) are labeled as $H_{F,1}$, $H_{F,2}$, $H_{F,3}$, ..., $H_{F,n}$, respectively. The formation enthalpy of each supercell is automatically calculated from HT first-principles calculations using the AFLOW framework.[35,36] We take the supercell with the lowest formation enthalpy as a reference (ground state structure) and denote its formation enthalpy as $H_{F,0}$. The relative formation enthalpy of the i^{th} supercell is calculated as $\Delta H_{F,i} = H_{F,i} - H_{F,0}$ and characterizes its disorder relative to the ground state. The probability P_i of the i^{th} supercell is determined by the Boltzmann factor

$$P_i = \frac{g_i e^{-\Delta H_{F,i}/k_B T}}{\sum_{i=1}^{n} g_i e^{-\Delta H_{F,i}/k_B T}}$$

where g_i is the degeneracy of the i^{th} supercell, $\Delta H_{F,i}$ is the relative formation enthalpy of the i^{th} supercell, k_B is the Boltzmann constant, and T is a virtual "roughness" temperature. T is not a true temperature per se but is instead a parameter describing how much disorder has been statistically explored during synthesis. To elaborate further, we consider two extremes in the ensemble average (ignoring structural degeneracy):

(1) $k_B T \lesssim \max(\Delta H_{F,i})$ neglecting highly disordered structures ($\Delta H_{F,i} \gg 0$) as $T \to 0$, and

(2) $k_B T \gg \max(\Delta H_{F,i})$ representing the annealed limit ($T \to \infty$) in which all structures are considered equiprobable.

The probability P_i describes the weight of the i^{th} supercell among the thermodynamically equivalent states of the disordered material at equilibrium.

2.4. Ensemble Average Density of States, Band Gap Energy, and Magnetic Moment. With the calculated material properties of each supercell and its equilibrium probability in hand, the overall system properties can be determined as ensemble averages of the properties calculated for each supercell. This work focuses on the calculation of the ensemble average density of states (DOS), band gap energy E_{gap}, and magnetic moment M. The DOS of the i^{th} supercell is labeled as $N_i(E)$ and indicates the number of electronic states per energy interval. The ensemble average DOS of the system is then determined by the formula

$$N(E) = \sum_{i=1}^{n} P_i \times N_i(E)$$

Additionally, a band gap $E_{gap,i}$ can be extracted from the DOS of each supercell. In this fashion, an ensemble average band gap E_{gap} can be calculated for the system. It is important to note that standard density functional theory (DFT) calculations are limited to a description of the ground state.[1−3] Subsequently, calculated excited state properties may contain substantial errors. In particular, DFT tends to underestimate the band gap.[47] Despite these known hindrances in the theory, we demonstrate in the next section that our framework is capable of predicting significant trends specific to the disordered systems. As a bonus, the calculation of these results are performed in a high-throughput fashion. It is expected that a more accurate, fine-grained description of the electronic structure in such systems will be obtained through a combination of our software framework and more advanced first-principles approaches.[48−54]

In the same spirit as the $N(E)$ and E_{gap}, we consider the calculation of the ensemble average magnetic moment M of the system. The magnetic moment of the i^{th} supercell is labeled as M_i. If the ground state of the i^{th} structure is spin-unpolarized, then its magnetic moment is set to zero, i.e., $M_i = 0$. Taking into account the impact of signed spins on the ensemble average, this approach is limited only to ferromagnetic solutions. Additionally, as an initialization for the self-consistent run, we assume the same ferromagnetic alignment among all of the spins in the system (an AFLOW calculation standard).[35] Finally, the ensemble average magnetic moment of the system is calculated with the formula

$$M = \sum_{i=1}^{n} P_i \times |M_i|$$

3. EXAMPLE APPLICATIONS

We analyze three disordered systems of technological importance using our framework: a zinc chalcogenide, a wide-gap oxide semiconductor, and an iron alloy. Unless otherwise stated, the supercells used in our calculations were generated with the lowest superlattice size n_{xct} needed to represent the composition exactly.

DOI: 10.1021/acs.chemmater.6b01449
Chem. Mater. 2016, 28, 6484−6492

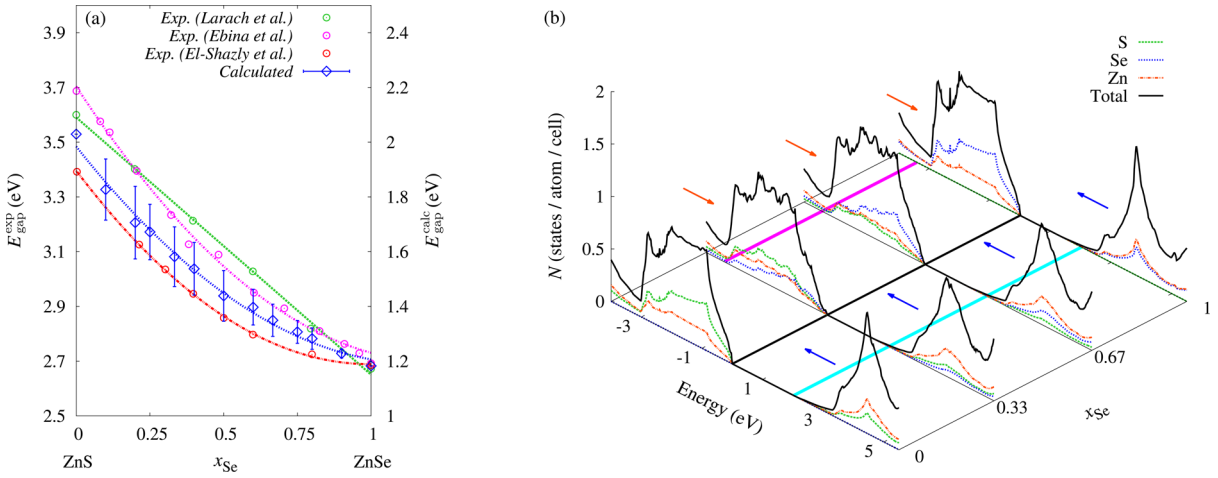

Figure 1. Disordered $ZnS_{1-x}Se_x$. (a) A comparison of the experimental[55−57] vs calculated compositional dependence of the band gap energy E_{gap} at room temperature. A rigid shift in the E_{gap} axis relative to the experimental results of ZnSe (second ordinate axis) accounts for the expected systematic deviation in DFT calculations.[47] Only the lowest empirical E_{gap} trends are shown. Error bars indicate the weighted standard deviation of the ensemble average E_{gap}. (b) Calculated density of states plots for various compositions: x_{Se} = 0.00 (n = 1), 0.33 (n = 3), 0.67 (n = 3), and 1.00 (n = 1). The straight black line indicates the position of the valence band maximum, and the straight magenta and cyan lines indicate the positions of the valence band minimum at x_{Se} = 0.33 and the conduction band minimum at x_{Se} = 0.00, respectively.

3.1. Zinc Chalcogenides. Over the years, zinc chalcogenides have garnered interest for a dynamic range of applications, beginning with the creation of the first blue-light-emitting laser diodes,[58] and have recently been studied as inorganic graphene analogues (IGAs) with potential applications in flexible and transparent nanodevices.[59] These wide-gap II−VI semiconductors have demonstrated a smoothly tunable band gap energy E_{gap} with respect to composition.[55−57] Both linear and quadratic dependencies have been observed with the latter phenomenon referred to as optical bowing.[60] Specifically, given the pseudoternary system $A_xB_{1-x}C$,

$$E_{gap}(x) = [x\epsilon_{AC} + (1 - x)\epsilon_{BC}] - bx(1 - x)$$

with b characterizing the bowing. Larach et al. reported a linear dependence (b = 0),[55] and Ebina et al.[56] and El-Shazly et al.[57] reported similar bowing parameters of b = 0.613 ± 0.027 and 0.457 ± 0.044 eV, respectively, averaged over the two observed direct transitions.

As a proof of concept, we utilized our developed disordered systems framework to calculate the compositional dependence of the E_{gap} and DOS for $ZnS_{1-x}Se_x$ at room temperature (annealed limit). Overall, this system shows relatively low disorder ($\max(\Delta H_{F,i}) \approx 0.005$ eV), exhibiting negligible variations in the ensemble average properties at higher temperatures. We compare these results, illustrated in Figure 1, to experimental measurements.[55−57] Common among all three trends (Figure 1(a)) is the E_{gap} shrinkage with increasing x_{Se}, as well as a near 1 eV tunable E_{gap} range. Our calculated trend demonstrates a nonzero bowing similar to that observed by both Ebina et al.[56] and El-Shazly et al.[57] A fit shows a bowing parameter of b = 0.585 ± 0.078 eV, lying in the range between the two experimental bowing parameters.

We also plot the ensemble average DOS plots at room temperature for x_{Se} = 0.00 (n = 1), 0.33 (n = 3), 0.67 (n = 3), and 1.00 (n = 1) in Figure 1(b). The plots echo the negatively correlated band gap relationship illustrated in Figure 1(a), highlighting that the replacement of sulfur with selenium atoms reduces the band gap. Specifically, we observe two phenomena as we increase the concentration of selenium: (red arrows) the reduction of the valence bandwidth (with the exception of x_{Se} = 0.00 (ZnS) concentration) and (blue arrows) a shift of the conduction band peak back toward the Fermi energy. The valence band of ZnS more closely resembles that of its extreme concentration counterpart at x_{Se} = 1.00 (ZnSe) than the others. The extreme concentration conduction peaks appear more defined than their intermediate concentration counterparts, which is likely an artifact of the ensemble averaging calculation.

Finally, we consider a partial-DOS analysis in both species and orbitals (not shown). In the valence band, sulfur and selenium account for the majority of the states in agreement with their relative concentrations. Meanwhile, zinc accounts for the majority of the states in the conduction band at all concentrations. Correspondingly, at all concentrations, the p-orbitals make up the majority of the valence band, whereas the conduction band consists primarily of s- and p-orbitals. These observations are consistent with conclusions drawn from previous optical reflectivity measurements that optical transitions are possible from sulfur or selenium valence bands to zinc conduction bands.[61]

Overall, our concentration-evolving E_{gap} trend and DOS plots support a continuing line of work[55−57] corroborating that this system is of the amalgamation type[62] and not of the persistence type.[61] Notably, however, reflectivity spectra shows that the peak position in the E_{gap} for ZnS-rich alloys may remain stationary,[56] which may have manifested itself in the aforementioned anomaly observed in this structure's valence bandwidth.

3.2. Wide-Gap Oxide Semiconductor Alloys. Zinc oxide (ZnO) has proven to be a pervasive material with far reaching applications such as paints, catalysts, pharmaceuticals (sun creams), and optoelectronics.[71] It has long been investigated for its electronic properties and falls into the class of transparent conducting oxides.[72] Just as our previous zinc chalcogenide example, ZnO is a wide-gap II−VI semiconductor that has demonstrated a tunable band gap energy E_{gap} with composition. In particular, ZnO has been engineered to have an E_{gap} range as large as 5 eV by synthesizing it with magnesium. This pairing has been intensively studied because of the likeness in ionic radius between zinc and magnesium, which results in mitigated

DOI: 10.1021/acs.chemmater.6b01449
Chem. Mater. 2016, 28, 6484−6492

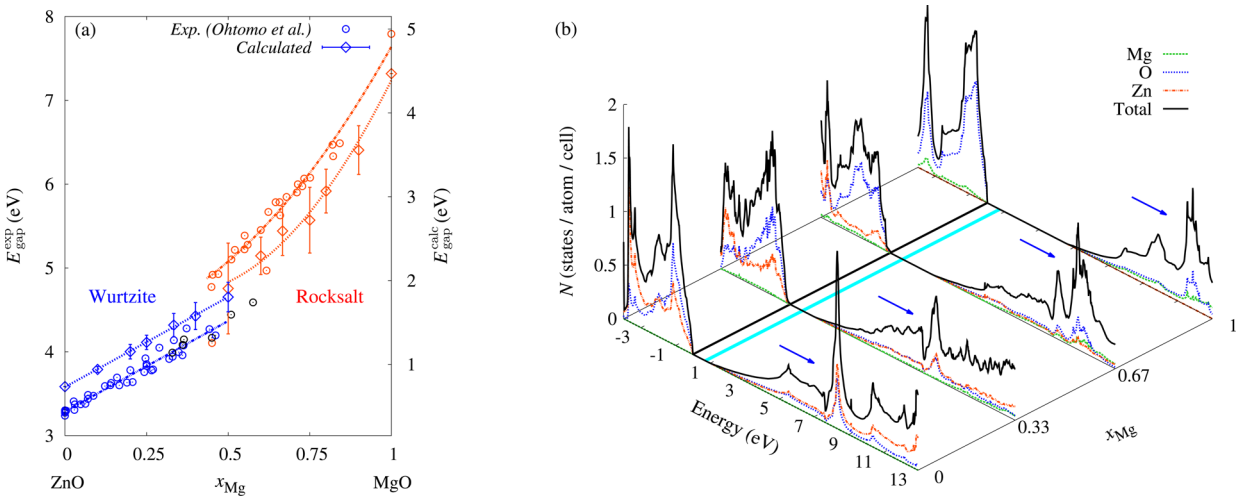

Figure 2. Disordered $Mg_xZn_{1-x}O$. (a) A comparison of the experimental[63−70] vs calculated compositional dependence of the band gap energy E_{gap} at room temperature. A rigid shift in the E_{gap} axis relative to the experimental results of MgO (second ordinate axis) accounts for the expected systematic deviation in DFT calculations.[47] The wurtzite and rocksalt structures are highlighted in blue and red, respectively, and the mixed phase structures are shown in black. Error bars indicate the weighted standard deviation of the ensemble average E_{gap}. (b) Calculated density of states plots for various compositions: x_{Mg} = 0.00 (n = 1), 0.33 (n = 3), 0.67 (n = 3), and 1.00 (n = 1). The straight black line indicates the position of the valence band maximum, and the straight cyan line indicates the position of the conduction band minimum at x_{Mg} = 0.00.

misfit strain in the heterostructure.[73] Although the solubility of MgO and ZnO is small, synthesis has been made possible throughout the full compositional spectrum.[63−70]

As another proof of concept, we model the compositional dependence of the E_{gap} and DOS for $Mg_xZn_{1-x}O$ at room temperature (annealed limit). In particular, we chose this disordered system to illustrate the breath of materials that this framework can model. Similar to $ZnS_{1-x}Se_x$, this system shows relatively low disorder ($\max(\Delta H_{F,i}) \approx 0.007$ eV), exhibiting negligible variations in the ensemble average properties at higher temperatures. We compare our results to those observed empirically[63−70] in Figure 2. As illustrated in Figure 2(a), Ohtomo et al. observed a composition-dependent phase transition from a wurtzite to a rocksalt structure with increasing x_{Mg}; the transition occurs around the mid concentrations. We mimic this transition in our calculations. Empirically, the overall trend in the wurtzite phase shows a negligible bowing in the E_{gap} trend, contrasting the significant bowing observed in the rocksalt phase. We note that the wurtzite phase E_{gap} trend shows a slope of 2.160 ± 0.080 eV, whereas the rocksalt phase shows a bowing parameter of 3.591 ± 0.856 eV. Calculated trends are shown in Figure 2(a). Qualitatively, we also observe linear and nonlinear E_{gap} trends in the wurtzite and rocksalt phases, respectively. The fits were as follows: we observe a slope of 2.147 ± 0.030 eV in the wurtzite phase and a bowing parameter of 5.971 ± 1.835 eV in the rocksalt phase. These trends match the experiment values well within the margins of error. We observe a larger margin of error in the rocksalt phase, particular in the phase-separated region ($0.4 \lesssim x_{Mg} \lesssim 0.6$). This may be indicative of the significant shear strain and complex nucleation behavior characterizing the region.[64]

We also plot the ensemble average DOS at room temperature for x_{Mg} = 0.00 (n = 1), 0.33 (n = 3), 0.67 (n = 3), and 1.00 (n = 1) in Figure 2(b). The plots not only echo the positively correlated band gap relationship illustrated in Figure 2(a) but also exhibit the aforementioned change from a linear to nonlinear trend. This is most easily seen by observing the shift in the conduction band away from the Fermi energy, highlighted by the blue arrows. Contrasting $ZnS_{1-x}Se_x$, we do not observe a significant change in width of the valence band as we vary the stoichiometry.

Finally, we consider a partial-DOS analysis in both species and orbitals (not shown). Overall, the constant oxygen backbone plays a major role in defining the shape of both the valence and conduction bands, particularly as x_{Mg} increases. This resonates with the strong p-orbital presence in both bands over all concentrations. Zinc and its d-orbitals play a particularly dominant role in the valence band in magnesium-poor structures.

3.3. Iron Alloys. Despite its ubiquity, iron remains at the focus of critical materials research. Even as new phenomena are discovered with an ever-growing effort to explore extreme conditions,[75−77] there exist long-standing, interesting aspects that are not fully resolved. This includes the magnetic character of the (fcc) γ-Fe phase at low temperatures,[78−80] among other complexities in its magnetic phase diagram.[81] One popular approach to studying the γ-Fe phase is through the $Fe_{1-x}Cu_x$ disordered alloy.[78,82,83] Nominally, unary copper and iron metals with fcc structures are nonmagnetic but together exhibit ferromagnetic ordering with very high magnetic moments. This observation has led to identification of Invar and anti-Invar behaviors, which may pave the way to enhanced thermomechanical actuators.[78,82] $Fe_{1-x}Cu_x$ is an interesting structure in its own right, as it has extremely low miscibility.[84] Overcoming the hurdle of developing metastable structures throughout the full compositional range has been the focus of much research.[85] Such metastable structures have demonstrated novel properties like high thermal and electrical conductivity,[86] magnetoresistance, and coercivity.[87]

As a final proof of concept, we model the compositional dependence of the magnetic moment M for $Fe_{1-x}Cu_x$ at T = 4.2 K for direct comparison against experimental results.[74] Considering both the sensitivity of magnetic properties to temperature as well as the significant disorder exhibited in this system ($\max(\Delta H_{F,i}) \approx 1.63$ eV), we limit our analysis to the low temperature limit. This is also where we expect our framework to perform optimally, which considers structures relaxed at zero temperature and pressure.[35] The results are

DOI: 10.1021/acs.chemmater.6b01449
Chem. Mater. 2016, 28, 6484−6492

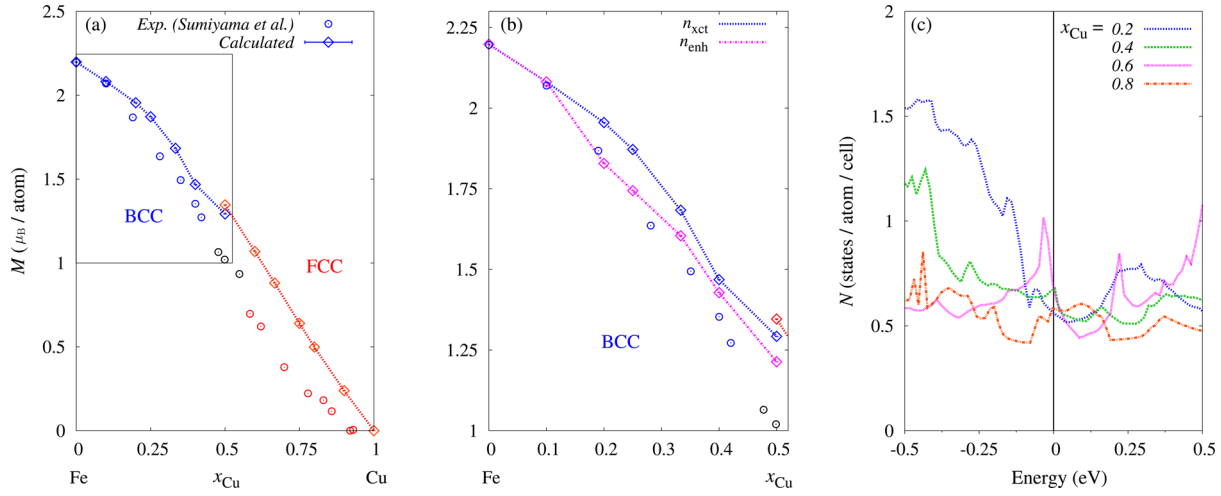

Figure 3. Disordered $Fe_{1-x}Cu_x$. (a) A comparison of the experimental[74] vs calculated compositional dependence of the magnetic moment M. Our calculations mimic the following phases observed at 4.2 K: $x_{Cu} \leq 0.42$ bcc phase shown in blue, $0.42 < x_{Cu} < 0.58$ mixed bcc-fcc phases shown in black, and $x_{Cu} \geq 0.58$ fcc phase shown in red. Error bars indicate the weighted standard deviation of the ensemble average E_{gap}. (b) A comparison of the aforementioned trends with calculations performed with enhanced superlattice sizes n_{enh}: $x_{Cu} = 0.00$ ($n_{xct} = 1$), 0.10 ($n_{xct} = 10$), 0.20 ($n_{xct} = 5$ vs $n_{enh} = 10$), 0.25 ($n_{xct} = 4$ vs $n_{enh} = 12$), 0.33 ($n_{xct} = 3$), 0.40 ($n_{xct} = 5$ vs $n_{enh} = 10$), and 0.50 ($n_{xct} = 2$ vs $n_{enh} = 10$). (c) Calculated spin-unpolarized density of states (DOS) plots at $x_{Cu} = 0.2$ ($n = 5$), 0.4 ($n = 5$), 0.6 ($n = 5$), and 0.8 ($n = 5$).

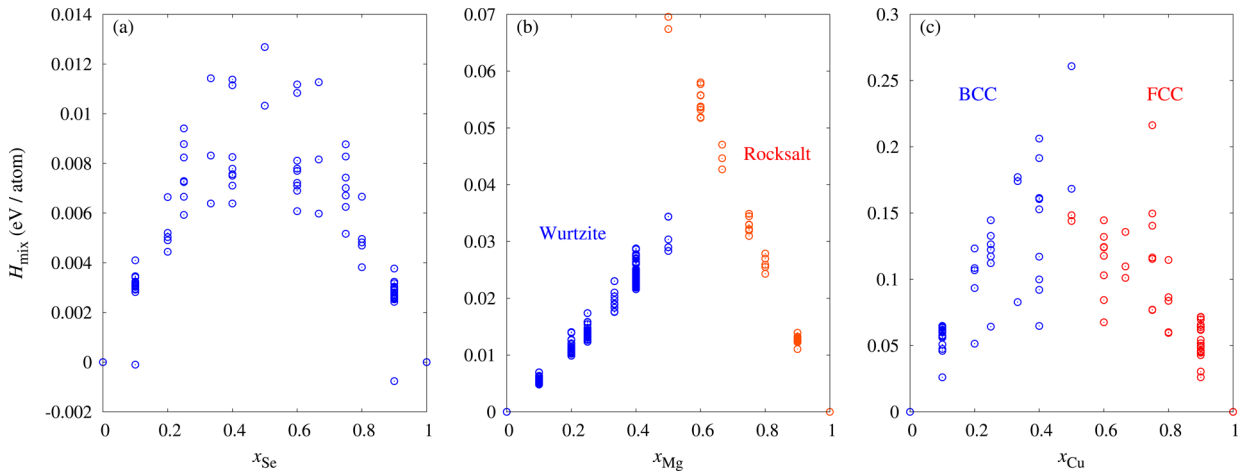

Figure 4. Mixing energy analyses[90] for the structures representing the three aforementioned disordered systems: (a) $ZnS_{1-x}Se_x$, (b) $Mg_xZn_{1-x}O$, and (c) $Fe_{1-x}Cu_x$.

illustrated in Figure 3. Sumiyama et al. show that the disordered system's phase is concentration dependent with a phase transition from bcc to fcc in the mid concentrations as x_{Cu} increases. Just as with $Mg_xZn_{1-x}O$, we mimic these observations in our calculations. The overall decreasing trend in M with reduced x_{Fe} in Figure 3(a) matches our expectations well.

With such a simple system, we also explore whether an augmented superlattice size n enhances our results. Although the concentration remains constant for n above that which is needed for the desired concentration n_{xct}, more structures are introduced into the ensemble average. The structures themselves also increase in size by a factor of n relative to their parent structure. For $x_{Cu} = 0.2$ and 0.4, we simply double n ($n_{enh} = 10$), and we triple n for $x_{Cu} = 0.25$ ($n_{enh} = 12$). With only two two-atom structures needed to describe $x_{Cu} = 0.5$ at n_{xct}, we were able to increase n by a factor of 5 ($n_{enh} = 10$) without compromising the feasibility of the calculation. A comparison of results calculated at n_{enh} is shown in Figure 3(b). At most concentrations, we observe substantial improvements as our calculated trend more closely follows that which was observed empirically.

Finally, we consider this system's ensemble average DOS in Figure 3(c). In general, the DOS near the Fermi energy decreases with increasing x_{Cu} with some instability near the mixed phase regions. This can be understood using the Stoner criterion model for transitional metals.[88,89] Namely, ferromagnetism appears when the gain in exchange energy is larger than the loss in kinetic energy. A larger DOS at the Fermi energy induces a higher exchange energy and favors a split into the ferromagnetic state. The competition between ferromagnetic and paramagnetic phases can be inferred from the decreasing M trend as depicted in Figure 3(a).

3.4. Thermodynamic Analysis. We explore the thermodynamic properties predicted by the framework for the three aforementioned disordered systems. Figure 4 shows the mixing energy analyses[90] for the representative enumerated structures. For $ZnS_{1-x}Se_x$, the mixing energies are only slightly positive: the mixing entropy should be enough to promote mixing even

DOI: 10.1021/acs.chemmater.6b01449
Chem. Mater. 2016, 28, 6484−6492

at low temperatures, overcoming the miscibility gap shown in previous experimental[55−57] and theoretical studies.[91] Meanwhile, $Mg_xZn_{1-x}O$ shows relatively small positive slopes in the mixing energies, implying the entropy at finite temperatures can realize non-negligible solubility of Mg in wurtzite-ZnO and Zn in rocksalt-MgO. This has certainly been verified experimentally in compositions outside of the $0.15 < x < 0.6$ two-phase region.[63] Finally, the mixing energies for $Fe_{1-x}Cu_x$ are mostly strongly positive, indicating only small solubilities of Cu in bcc-Fe and Fe in fcc-Cu are possible at finite temperatures, which is also in agreement with experimental values.[74,84]

4. SOFTWARE

The automated approach to model disordered systems discussed here is implemented within the AFLOW framework[35,36] and can be downloaded from http://aflow.org.

5. CONCLUSIONS

In this work, we have introduced a software framework capable of modeling substitutionally disordered materials. Specifically, the framework delivers high value properties of disordered systems, including the density of states (DOS), band gap energy E_{gap}, and magnetic moment M, as well as additional insight into underlying physical mechanisms. Through a number of technologically significant examples, we have illustrated the prowess of this highly efficient and convenient framework. Such materials that exhibit highly tunable properties are of critical importance toward the goal of rational materials design. Without loss of feasibility or accuracy, the framework exploits highly successful high-throughput first-principles approaches in more complex, real-world systems.

■ ASSOCIATED CONTENT

Supporting Information

The Supporting Information is available free of charge on the ACS Publications website at DOI: 10.1021/acs.chemmater.6b01449.

Full description and an example of the PARTCAR file for disordered system $Ag_{8.733}Cd_{3.8}Zr_{3.267}$, a depiction of this disordered system using VESTA,[92] a figure illustrating the variation of the band gap energy E_{gap} as a function of the superlattice size n, and a summary of the computational times for each system (PDF)

■ AUTHOR INFORMATION

Corresponding Author

*E-mail: stefano@duke.edu.

Notes

The authors declare no competing financial interest.

■ ACKNOWLEDGMENTS

We thank D. J. Hicks, J. J. Plata, C. Toher, M. Buongiorno Nardelli, and M. Fornari for various technical discussions that have contributed to the results reported in this article. This work was supported by ONR-MURI under Contract N00014-13-1-0635, DOD ONR (N00014-14-1-0526 and N00014-11-1-0136), and the Duke University Center for Materials Genomics. K.Y. acknowledges support by start-up funds from the University of California San Diego. C.O. acknowledges support from the National Science Foundation Graduate Research Fellowship under Grant No. DGF1106401. We also acknowledge the CRAY corporation for computational support.

■ REFERENCES

(1) Kohn, W.; Sham, L. J. Self-Consistent Equations Including Exchange and Correlation Effects. *Phys. Rev.* **1965**, *140*, A1133.
(2) Hohenberg, P.; Kohn, W. Inhomogeneous Electron Gas. *Phys. Rev.* **1964**, *136*, B864−B871.
(3) Curtarolo, S.; Hart, G. L. W.; Buongiorno Nardelli, M.; Mingo, N.; Sanvito, S.; Levy, O. The High-Throughput Highway to Computational Materials Design. *Nat. Mater.* **2013**, *12*, 191−201.
(4) Elliott, S. R. *Physics of Amorphous Materials*; Longman Scientific & Technical: New York, 1990.
(5) Xie, L.; Brault, P.; Coutanceau, C.; Bauchire, J.-M.; Caillard, A.; Baranton, S.; Berndt, J.; Neyts, E. C. Efficient Amorphous Platinum Catalyst Cluster Growth on Porous Carbon: A Combined Molecular Dynamics and Experimental Study. *Appl. Catal., B* **2015**, *162*, 21−26.
(6) Kurian, S.; Seo, H.; Jeon, H. Significant Enhancement in Visible Light Absorption of TiO_2 Nanotube Arrays by Surface Band Gap Tuning. *J. Phys. Chem. C* **2013**, *117*, 16811−16819.
(7) Bednorz, J. G.; Müller, K. A. Possible High T_c Superconductivity in the Ba-La-Cu-O System. *Z. Phys. B: Condens. Matter* **1986**, *64*, 189−193.
(8) Maeno, Y.; Hashimoto, H.; Yoshida, K.; Nishizaki, S.; Fujita, T.; Bednorz, J. G.; Lichtenberg, F. Superconductivity in a Layered Perovskite Without Copper. *Nature* **1994**, *372*, 532−534.
(9) Winter, M. R.; Clarke, D. R. Oxide Materials with Low Thermal Conductivity. *J. Am. Ceram. Soc.* **2007**, *90*, 533−540.
(10) Patra, N. C.; Bharatan, S.; Li, J.; Tilton, M.; Iyer, S. Molecular Beam Epitaxial Growth and Characterization of $InSb_{1-x}N_x$ on GaAs for Long Wavelength Infrared Applications. *J. Appl. Phys.* **2012**, *111*, 083104.
(11) Wang, H.; Zhang, Y. N.; Wu, R. Q.; Sun, L. Z.; Xu, D. S.; Zhang, Z. D. Understanding Strong Magnetostriction in $Fe_{100-x}Ga_x$ Alloys. *Sci. Rep.* **2013**, *3*, 1.
(12) Pussi, K.; Ferralis, N.; Mihalkovič, M.; Widom, M.; Curtarolo, S.; Gierer, M.; Jenks, C. J.; Canfield, P.; Fisher, I. R.; Diehl, R. D. Use of Periodic Approximants in a Dynamical LEED Study of the Quasicrystalline Tenfold Surface of Decagonal Al-Ni-Co. *Phys. Rev. B: Condens. Matter Mater. Phys.* **2006**, *73*, 184203.
(13) Mihalkovič, M.; Widom, M. Tile Decoration Model of the W-(Al-Co-Ni) Approximant. *Philos. Mag.* **2006**, *86*, 557−565.
(14) Faulkner, J. S. The Modern Theory of Alloys. *Prog. Mater. Sci.* **1982**, *27*, 1−187.
(15) Nordheim, L. Zur Elektronentheorie Der Metalle I. *Ann. Phys.* **1931**, *401*, 607−640.
(16) Bellaiche, L.; Vanderbilt, D. Virtual Crystal Approximation Revisited: Application to Dielectric and Piezoelectric Properties of Perovskites. *Phys. Rev. B: Condens. Matter Mater. Phys.* **2000**, *61*, 7877−7882.
(17) Ramer, N. J.; Rappe, A. M. Virtual-Crystal Approximation That Works: Locating a Composition Phase Boundary in $Pb(Zr_{1-x}Ti_3)O_3$. arXiv:9909032v3 [cond-mat.mtrl-sci], 2000.
(18) Soven, P. Coherent-Potential Model of Substitutional Disordered Alloys. *Phys. Rev.* **1967**, *156*, 809−813.
(19) Korringa, J. On the Calculation of the Energy of a Bloch Wave in a Metal. *Physica* **1947**, *13*, 392−400.
(20) Kohn, W.; Rostoker, N. Solution of the Schrödinger Equation in Periodic Lattices with an Application to Metallic Lithium. *Phys. Rev.* **1954**, *94*, 1111−1120.
(21) Ebert, H.; Ködderitzsch, D.; Minár, J. Calculating Condensed Matter Properties Using the KKR-Green's Function Method−Recent Developments and Applications. *Rep. Prog. Phys.* **2011**, *74*, 096501.
(22) Stocks, G. M.; Temmerman, W. M.; Györffy, B. L. Complete Solution of the Korringa-Kohn-Rostoker Coherent-Potential-Approximation Equations: Cu-Ni Alloys. *Phys. Rev. Lett.* **1978**, *41*, 339−343.
(23) Rowlands, D. A.; Staunton, J. B.; Györffy, B. L. Korringa-Kohn-Rostoker Nonlocal Coherent-Potential Approximation. *Phys. Rev. B: Condens. Matter Mater. Phys.* **2003**, *67*, 115109.

DOI: 10.1021/acs.chemmater.6b01449
Chem. Mater. 2016, 28, 6484−6492

(24) Zunger, A.; Wei, S.-H.; Ferreira, L. G.; Bernard, J. E. Special Quasirandom Structures. *Phys. Rev. Lett.* **1990**, *65*, 353−356.
(25) Ma, J.; Deng, H.-X.; Luo, J.-W.; Wei, S.-H. Origin of the Failed Ensemble Average Rule for the Band Gaps of Disordered Non-isovalent Semiconductor Alloys. *Phys. Rev. B: Condens. Matter Mater. Phys.* **2014**, *90*, 115201.
(26) Capaz, R. B.; Koiller, B. Partial-Ordering Effects in $In_xGa_{1-x}P$. *Phys. Rev. B: Condens. Matter Mater. Phys.* **1993**, *47*, 4044−4047.
(27) Zhang, Y.; Mascarenhas, A.; Wang, L.-W. Dependence of the Band Structure on the Order Parameter for Partially Ordered $Ga_xIn_{1-x}P$ Alloys. *Phys. Rev. B: Condens. Matter Mater. Phys.* **2001**, *63*, 201312.
(28) Zhang, Y.; Mascarenhas, A.; Wang, L.-W. Statistical Aspects of Electronic and Structural Properties in Partially Ordered Semiconductor Alloys. *Phys. Rev. B: Condens. Matter Mater. Phys.* **2001**, *64*, 125207.
(29) Grau-Crespo, R.; Hamad, S.; Catlow, C. R. A.; de Leeuw, N. H. Symmetry-Adapted Configurational Modelling of Fractional Site Occupancy in Solids. *J. Phys.: Condens. Matter* **2007**, *19*, 256201.
(30) Mourad, D.; Czycholl, G.; Kruse, C.; Klembt, S.; Retzlaff, R.; Hommel, D.; Gartner, M.; Anastasescu, M. Band Gap Bowing of Binary Alloys: Experimental Results Compared to Theoretical Tight-Binding Supercell Calculations for $Cd_xZn_{1-x}Se$. *Phys. Rev. B: Condens. Matter Mater. Phys.* **2010**, *82*, 165204.
(31) Habgood, M.; Grau-Crespo, R.; Price, S. L. Substitutional and Orientational Disorder in Organic Crystals: A Symmetry-Adapted Ensemble Model. *Phys. Chem. Chem. Phys.* **2011**, *13*, 9590−9600.
(32) Haverkort, M. W.; Elfimov, I. S.; Sawatzky, G. A. Electronic Structure and Self Energies of Randomly Substituted Solids Using Density Functional Theory and Model Calculations. arXiv:1109.4036v1 [cond-mat.mtrl-sci], 2011.
(33) Eckhardt, C.; Hummer, K.; Kresse, G. Indirect-to-Direct Gap Transition in Strained and Unstrained Sn_xGe_{1-x} Alloys. *Phys. Rev. B: Condens. Matter Mater. Phys.* **2014**, *89*, 165201.
(34) Office of Science and Technology Policy, White House, Materials Genome Initiative for Global Competitiveness. http://www.whitehouse.gov/mgi, 2011.
(35) Calderon, C. E.; Plata, J. J.; Toher, C.; Oses, C.; Levy, O.; Fornari, M.; Natan, A.; Mehl, M. J.; Hart, G. L. W.; Buongiorno Nardelli, M.; Curtarolo, S. The AFLOW Standard for High-Throughput Materials Science Calculations. *Comput. Mater. Sci.* **2015**, *108 Part A*, 233−238.
(36) Curtarolo, S.; Setyawan, W.; Hart, G. L. W.; Jahnátek, M.; Chepulskii, R. V.; Taylor, R. H.; Wang, S.; Xue, J.; Yang, K.; Levy, O.; Mehl, M. J.; Stokes, H. T.; Demchenko, D. O.; Morgan, D. AFLOW: An Automatic Framework for High-Throughput Materials Discovery. *Comput. Mater. Sci.* **2012**, *58*, 218−226.
(37) Rappe, A. K.; Casewit, C. J.; Colwell, K. S.; Goddard, W. A.; Skiff, W. M. UFF, A Full Periodic Table Force Field for Molecular Mechanics and Molecular Dynamics Simulations. *J. Am. Chem. Soc.* **1992**, *114*, 10024−10035.
(38) Setyawan, W.; Curtarolo, S. High-Throughput Electronic Band Structure Calculations: Challenges and Tools. *Comput. Mater. Sci.* **2010**, *49*, 299−312.
(39) Kresse, G.; Furthmüller, J. Efficiency of Ab-Initio Total Energy Calculations for Metals and Semiconductors Using a Plane-Wave Basis Set. *Comput. Mater. Sci.* **1996**, *6*, 15.
(40) Kresse, G.; Furthmüller, J. Efficient Iterative Schemes for *Ab Initio* Total-Energy Calculations Using a Plane-Wave Basis Set. *Phys. Rev. B: Condens. Matter Mater. Phys.* **1996**, *54*, 11169−11186.
(41) Hart, G. L. W.; Forcade, R. W. Algorithm for Generating Derivative Structures. *Phys. Rev. B: Condens. Matter Mater. Phys.* **2008**, *77*, 224115.
(42) Hart, G. L. W.; Forcade, R. W. Generating Derivative Structures from Multilattices: Algorithm and Application to HCP Alloys. *Phys. Rev. B: Condens. Matter Mater. Phys.* **2009**, *80*, 014120.
(43) Hart, G. L. W.; Nelson, L. J.; Forcade, R. W. Generating Derivative Structures at a Fixed Concentration. *Comput. Mater. Sci.* **2012**, *59*, 101−107.
(44) Goedecker, S. Minima Hopping: An Efficient Search Method for the Global Minimum of the Potential Energy Surface of Complex Molecular Systems. *J. Chem. Phys.* **2004**, *120*, 9911−9917.
(45) Hautier, G.; Fischer, C. C.; Jain, A.; Mueller, T.; Ceder, G. Finding Nature's Missing Ternary Oxide Compounds Using Machine Learning and Density Functional Theory. *Chem. Mater.* **2010**, *22*, 3762−3767.
(46) Lacivita, V.; Erba, A.; Dovesi, R.; D'Arco, P. Elasticity of Grossular-Andradite Solid Solution: An *Ab Initio* Investigation. *Phys. Chem. Chem. Phys.* **2014**, *16*, 15331−15338.
(47) Perdew, J. P. Density Functional Theory and the Band Gap Problem. *Int. J. Quantum Chem.* **1985**, *28*, 497−523.
(48) Aryasetiawan, F.; Gunnarsson, O. The GW Method. *Rep. Prog. Phys.* **1998**, *61*, 237.
(49) Hedin, L. New Method for Calculating the One-Particle Green's Function with Application to the Electron-Gas Problem. *Phys. Rev.* **1965**, *139*, A796−A823.
(50) Heyd, J.; Scuseria, G. E.; Ernzerhof, M. Hybrid Functionals Based on a Screened Coulomb Potential. *J. Chem. Phys.* **2003**, *118*, 8207−8215.
(51) Liechtenstein, A. I.; Anisimov, V. I.; Zaanen, J. Density-Functional Theory and Strong Interactions: Orbital Ordering in Mott-Hubbard Insulators. *Phys. Rev. B: Condens. Matter Mater. Phys.* **1995**, *52*, R5467−R5470.
(52) Agapito, L. A.; Ferretti, A.; Calzolari, A.; Curtarolo, S.; Buongiorno Nardelli, M. Effective and Accurate Representation of Extended Bloch States on Finite Hilbert Spaces. *Phys. Rev. B: Condens. Matter Mater. Phys.* **2013**, *88*, 165127.
(53) Agapito, L. A.; Curtarolo, S.; Buongiorno Nardelli, M. Reformulation of DFT + *U* as a Pseudohybrid Hubbard Density Functional for Accelerated Materials Discovery. *Phys. Rev. X* **2015**, *5*, 011006.
(54) Gopal, P.; Fornari, M.; Curtarolo, S.; Agapito, L. A.; Liyanage, L. S. I.; Buongiorno Nardelli, M. Improved Predictions of the Physical Properties of Zn- and Cd-based Wide Band-Gap Semiconductors: A Validation of the ACBN0 Functional. *Phys. Rev. B: Condens. Matter Mater. Phys.* **2015**, *91*, 245202.
(55) Larach, S.; Shrader, R. E.; Stocker, C. F. Anomalous Variation of Band Gap with Composition in Zinc Sulfo- and Seleno-Tellurides. *Phys. Rev.* **1957**, *108*, 587−589.
(56) Ebina, A.; Fukunaga, E.; Takahashi, T. Variation with Composition of the E_0 and $E_0+\Delta_0$ Gaps in ZnS_xSe_{1-x} Alloys. *Phys. Rev. B* **1974**, *10*, 2495−2500.
(57) El-Shazly, A. A.; El-Naby, M. M. H.; Kenawy, M. A.; El-Nahass, M. M.; El-Shair, H. T.; Ebrahim, A. M. Optical Properties of Ternary ZnS_xSe_{1-x} Polycrystalline Thin Films. *Appl. Phys. A: Solids Surf.* **1985**, *36*, 51−53.
(58) Haase, M. A.; Qiu, J.; DePuydt, J. M.; Cheng, H. Blue-Green Laser Diodes. *Appl. Phys. Lett.* **1991**, *59*, 1272−1274.
(59) Sun, Y.; Sun, Z.; Gao, S.; Cheng, H.; Liu, Q.; Piao, J.; Yao, T.; Wu, C.; Hu, S.; Wei, S.; Xie, Y. Fabrication of Flexible and Freestanding Zinc Chalcogenide Single Layers. *Nat. Commun.* **2012**, *3*, 1057.
(60) Bernard, J. E.; Zunger, A. Optical Bowing in Zinc Chalcogenide Semiconductor Alloys. *Phys. Rev. B: Condens. Matter Mater. Phys.* **1986**, *34*, 5992−5995.
(61) Kirschfeld, K. E.; Nelkowski, N.; Wagner, T. S. Optical Reflectivity and Band Structure of $ZnS_{1-x}Se_x$ Mixed Crystals. *Phys. Rev. Lett.* **1972**, *29*, 66−68.
(62) Onodera, Y.; Toyozawa, Y. Persistence and Amalgamation Types in the Electronic Structure of Mixed Crystals. *J. Phys. Soc. Jpn.* **1968**, *24*, 341−355.
(63) Ohtomo, A.; Tsukazaki, A. Pulsed Laser Deposition of Thin Films and Superlattices Based on ZnO. *Semicond. Sci. Technol.* **2005**, *20*, S1.
(64) Takeuchi, I.; Yang, W.; Chang, K.-S.; Aronova, M. A.; Venkatesan, T.; Vispute, R. D.; Bendersky, L. A. Monolithic Multichannel Ultraviolet Detector Arrays and Continuous Phase

DOI: 10.1021/acs.chemmater.6b01449
Chem. Mater. 2016, 28, 6484−6492

Evolution in $Mg_xZn_{1-x}O$ Composition Spreads. *J. Appl. Phys.* **2003**, *94*, 7336−7340.
(65) Chen, J.; Shen, W. Z.; Chen, N. B.; Qiu, D. J.; Wu, H. Z. The Study of Composition Non-Uniformity in Ternary $Mg_xZn_{1-x}O$ Thin Films. *J. Phys.: Condens. Matter* **2003**, *15*, L475.
(66) Takagi, T.; Tanaka, H.; Fujita, S.; Fujita, S. Molecular Beam Epitaxy of High Magnesium Content Single-Phase Wurzite $Mg_xZn_{1-x}O$ Alloys ($x \simeq 0.5$) and Their Application to Solar-Blind Region Photodetectors. *Jpn. J. Appl. Phys.* **2003**, *42*, L401.
(67) Choopun, S.; Vispute, R. D.; Yang, W.; Sharma, R. P.; Venkatesan, T.; Shen, H. Realization of Band Gap Above 5.0 eV in Metastable Cubic-Phase $Mg_xZn_{1-x}O$ Alloy Films. *Appl. Phys. Lett.* **2002**, *80*, 1529−1531.
(68) Minemoto, T.; Negami, T.; Nishiwaki, S.; Takakura, H.; Hamakawa, Y. Preparation of $Zn_{1-x}Mg_xO$ Films by Radio Frequency Magnetron Sputtering. *Thin Solid Films* **2000**, *372*, 173−176.
(69) Sharma, A. K.; Narayan, J.; Muth, J. F.; Teng, C. W.; Jin, C.; Kvit, A.; Kolbas, R. M.; Holland, O. W. Optical and Structural Properties of Epitaxial $Mg_xZn_{1-x}O$ Alloys. *Appl. Phys. Lett.* **1999**, *75*, 3327−3329.
(70) Ohtomo, A.; Kawasaki, M.; Koida, T.; Masubuchi, K.; Koinuma, H.; Sakurai, Y.; Yoshida, Y.; Yasuda, T.; Segawa, Y. $Mg_xZn_{1-x}O$ as a II-VI Widegap Semiconductor Alloy. *Appl. Phys. Lett.* **1998**, *72*, 2466−2468.
(71) Takeuchi, I.; Yang, W.; Chang, K. S.; Vispute, R. D.; Venkatesan, T. V. System and Method of Fabrication and Application of Thin-Films with Continuously Graded or Discrete Physical Property Parameters to Functionally Broadband Monolithic Microelectronic Optoelectronic/Sensor/Actuator Device Arrays. 2007; US Patent 7,309,644.
(72) Ellmer, K.; Klein, A.; Rech, B. *Transparent Conductive Zinc Oxide: Basics and Applications in Thin Film Solar Cells*; Springer Series in Materials Science; Springer: Berlin Heidelberg, 2007.
(73) Yoo, S. J.; Lee, J.-H.; Kim, C.-Y.; Kim, C. H.; Shin, J. W.; Kim, H. S.; Kim, J.-G. Direct Observation of the Crystal Structure Changes in the $Mg_xZn_{1-x}O$ Alloy System. *Thin Solid Films* **2015**, *588*, 50−55.
(74) Sumiyama, K.; Yoshitake, T.; Nakamura, Y. Magnetic Properties of Metastable BCC and FCC Fe-Cu Alloys Produced by Vapor Quenching. *J. Phys. Soc. Jpn.* **1984**, *53*, 3160−3165.
(75) Bonetti, E.; Del Bianco, L.; Fiorani, D.; Rinaldi, D.; Caciuffo, R.; Hernando, A. Disordered Magnetism at the Grain Boundary of Pure Nanocrystalline Iron. *Phys. Rev. Lett.* **1999**, *83*, 2829−2832.
(76) Shimizu, K.; Kimura, T.; Furomoto, S.; Takeda, K.; Kontani, K.; Onuki, Y.; Amaya, K. Superconductivity in the Non-Magnetic State of Iron Under Pressure. *Nature* **2001**, *412*, 316−318.
(77) Bose, S. K.; Dolgov, O. V.; Kortus, J.; Jepsen, O.; Andersen, O. K. Pressure Dependence of Electron-Phonon Coupling and Superconductivity in HCP Fe: A Linear Response Study. *Phys. Rev. B: Condens. Matter Mater. Phys.* **2003**, *67*, 214518.
(78) Gorria, P.; Martínez-Blanco, D.; Blanco, J. A.; Hernando, A.; Garitaonandia, J. S.; Barquín, L. F.; Campo, J.; Smith, R. I. Invar Effect in FCC-FeCu Solid Solutions. *Phys. Rev. B: Condens. Matter Mater. Phys.* **2004**, *69*, 214421.
(79) Abrahams, S. C.; Guttman, L.; Kasper, J. S. Neutron Diffraction Determination of Antiferromagnetism in Face-Centered Cubic (γ) Iron. *Phys. Rev.* **1962**, *127*, 2052−2055.
(80) Sandratskii, L. M. Noncollinear Magnetism in Itinerant-Electron Systems: Theory and Applications. *Adv. Phys.* **1998**, *47*, 91−160.
(81) Pepperhoff, W.; Acet, M. *Constitution and Magnetism of Iron and Its Alloys*; Engineering Materials; Springer: Berlin Heidelberg, 2001.
(82) Gorria, P.; Martínez-Blanco, D.; Blanco, J. A.; Pérez, M. J.; Hernando, A.; Barquín, L. F.; Smith, R. I. High-Temperature Induced Ferromagnetism on γ−Fe Precipitates in FeCu Solid Solutions. *Phys. Rev. B: Condens. Matter Mater. Phys.* **2005**, *72*, 014401.
(83) Orecchini, A.; Sacchetti, F.; Petrillo, C.; Postorino, P.; Congeduti, A.; Giorgetti, Ch.; Baudelet, F.; Mazzone, G. Magnetic States of Iron in Metastable FCC Fe-Cu Alloys. *J. Alloys Compd.* **2006**, *424*, 27−32.
(84) Liu, J. Z.; van de Walle, A.; Ghosh, G.; Asta, M. Structure, Energetics, and Mechanical Stability of Fe-Cu BCC Alloys from First-Principles Calculations. *Phys. Rev. B: Condens. Matter Mater. Phys.* **2005**, *72*, 144109.
(85) Ma, E. Alloys Created Between Immiscible Elements. *Prog. Mater. Sci.* **2005**, *50*, 413−509.
(86) Korn, D.; Pfeifle, H.; Niebuhr, J. Electrical Resistivity of Metastable Copper-Iron Solid Solutions. *Z. Phys. B: Condens. Matter Quanta* **1976**, *23*, 23−26.
(87) Hihara, T.; Xu, Y.; Konno, T. J.; Sumiyama, K.; Onodera, H.; Wakoh, K.; Suzuki, K. Microstructure and Giant Magnetoresistance in Fe-Cu Thin Films Prepared by Cluster-Beam Deposition. *Jpn. J. Appl. Phys.* **1997**, *36*, 3485.
(88) Xie, Y.-P.; Zhao, S.-J. The Energetic and Structural Properties of BCC NiCu, FeCu Alloys: A First-Principles Study. *Comput. Mater. Sci.* **2011**, *50*, 2586−2591.
(89) James, P.; Eriksson, O.; Johansson, B.; Abrikosov, I. A. Calculated Magnetic Properties of Binary Alloys Between Fe, Co, Ni, and Cu. *Phys. Rev. B: Condens. Matter Mater. Phys.* **1999**, *59*, 419−430.
(90) Usanmaz, D.; Nath, P.; Plata, J. J.; Hart, G. L. W.; Takeuchi, I.; Buongiorno Nardelli, M.; Fornari, M.; Curtarolo, S. First Principles Thermodynamical Modelingof the Binodal and Spinodal Curves in Lead Chalcogenides. *Phys. Chem. Chem. Phys.* **2016**, *18*, 5005−5011.
(91) Janetzko, F.; Jug, K. Miscibility of Zinc Chalcogenides. *J. Phys. Chem. A* **2004**, *108*, 5449−5453.
(92) Momma, K.; Izumi, F. *VESTA3* for Three-Dimensional Visualization of Crystal, Volumetric and Morphology Data. *J. Appl. Crystallogr.* **2011**, *44*, 1272−1276.

DOI: 10.1021/acs.chemmater.6b01449
Chem. Mater. 2016, 28, 6484−6492